Title

Tracking surface photovoltage dipole geometry in Bi2Se3 with time-resolved photoemission

Journal

Journal of Statistical Mechanics Theory and Experiment, 2019(10)

ISSN

1742-5468

Authors

Ciocys, S
Morimoto, T
Moore, JE
et al.

Publication Date

2019-10-01

DOI

10.1088/1742-5468/ab458a

Peer reviewed

Journal of Statistical Mechanics:
Theory and Experiment

SISSA

NESMCQ18

Tracking surface photovoltage dipole geometry in Bi_2Se_3 with time-resolved photoemission

Journal of Statistical Mechanics: Theory and Experiment
An IOP and SISSA journal

Tracking surface photovoltage dipole geometry in Bi_2Se_3 with time-resolved photoemission

S Ciocys[1,2], T Morimoto[1], J E Moore[1,2] and A Lanzara[1,2]

[1] Department of Physics, University of California, Berkeley, CA 94720, United States of America
[2] Materials Sciences Division, Lawrence Berkeley National Laboratory, Berkeley, CA 94720, United States of America
E-mail: alanzara@lbl.gov

Received 15 July 2019
Accepted for publication 15 September 2019
Published 16 October 2019

Online at stacks.iop.org/JSTAT/2019/104008
https://doi.org/10.1088/1742-5468/ab458a

Abstract. Topological insulators have been shown to exhibit strong and long-lived surface photovoltages when excited by an infrared pump. The ability to generate long-lived potentials on these surfaces provides opportunities to manipulate the spin-momentum locked topological surface states. Moreover, the photo-induced nature of this effect allows for localized excitation of arbitrary geometries. Knowing precisely how these potentials form and evolve is critical in understanding how to manage the effect in applications. The uniqueness of the photoemission experimental geometry, in which the photoelectron must traverse the induced surface field in vacuum, provides an interesting probe of the electric dipole shape generated by the surface photovoltage. In this study, we are able to match the observed decay of the geometric effect on the photoelectron to an essential electrodynamics model of the light-induced dipole thereby tracking the fluence-dependent evolution of the dipole geometry. By utilizing a standard time-resolved angle-resolved photoemission experiment, we are able to determine real-space information of the dipole while simultaneously recovering time-resolved band structure.

Keywords: surface effects, surface spectroscopy, STM etc, topological insulators, topological phases of matter

1742-5468/19/104008+11$33.00

Contents

Introduction

The negative-delay spectra in time and angle-resolved photoemission spectroscopy (T-ARPES), in which the photoemitting probe arrives before the pump, are typically used to characterize equilibrium band structure [1–5]. However, in situations in which the pumped non-equilibrium state hosts a time-dependent electric field, the negative delay exhibits non-equilibrium behavior that is dependent on the magnitude, time-scale, and, most importantly, the geometry of the excitation [6–8].

An example of a pump-induced excitation that results in a time-dependent electric field is the surface photovoltage (SPV) effect [6, 9–11]. An SPV forms in a semiconducting system that exhibits bulk-to-surface band bending. In-gap states at the surface facilitate a charge redistribution between the surface and bulk in order to establish a flat chemical potential. This results in a non-uniform charge distribution and therefore an internal electric field that bends the surface bands. Upon illumination, photoexcited charges cancel the internal field, reversibly reducing the band bending [12–13].

The necessary ingredients for an SPV are a Fermi level in the bulk gap and in-gap surface states [12–13]. Topological insulators are ideal SPV candidates. They host topologically-protected in-gap surface states and are bulk-insulating as long as they are doped into the bulk gap [14–17]. In recent years, many topological insulator systems have been reported to exhibit SPVs via T-ARPES [9–11]. During the topological SPV excitation, the surface band bending is mitigated driving a potential difference between the spin-momentum locked surface states inside and outside the excited regions on the surface. This phenomenon opens doors for possible applications such as light-induced spin-current switches or a means to drive localized spin-currents [18–20].

The pump-induced SPV can be measured directly with T-ARPES [6, 8–11]. Upon illumination, the band structure rigidly shifts as the non-equilibrium chemical potential tracks the band bending reduction. For positive delays (in which the probe arrives progressively later after the pump) the excitation decays and the band structure shift diminishes. Naively, one would expect the negative delay to exhibit only equilibrium behavior. However, at negative delays near temporal overlap at delay $= 0$ ps, the band structure is also shifted and this shift decays at further negative delays. This phenomenon is due to the ARPES geometry, in which the photo-emitted electron must

J. Stat. Mech. (2019) 104008

propagate through vacuum to the detector. At negative delays, the photoelectron is emitted first, the pump arrives after the delay time, and the generated field provides an impulse to the traveling electron which shifts the observed binding energy. In this way, the negative delay is governed by the generated electric field shape in vacuum which is in turn determined by the shape of the generated dipole [6–8].

In this study we examine the fluence-dependent SPV dipole evolution in Bi_2Se_3. We employ the negative-delay electric field model developed by Yang *et al* [6], but with non-Gaussian dipoles and demonstrate that the negative delay is an effective region for determining dipole geometry in T-ARPES experiments.

Results

We start our study by examining the difference in pump–probe excitations between bulk-conductive (Fermi level doped into the bulk-conduction band) and bulk-insulating (Fermi level doped into the bulk gap) Bi_2Se_3 bulk crystals. The bulk-insulating Bi_2Se_3 have been bulk-doped with magnesium to establish an in-gap Fermi level. We utilized 800 nm pump pulses with ∼150 fs pulse duration. Figure 1 demonstrates the markedly different behavior between these two systems. The cartoons in figure 1(a) illustrate the difference in doping between the two samples. In the bulk-insulating case (lower cartoon), the Fermi-level is in the bulk gap (bands deep in the bulk shown in light grey), and the bulk bands at the surface (dark grey) as well as the topological surface state (red and blue) are shifted downward by band bending. This can be seen by the offset of the bulk valence band in light grey and the surface valence band in dark grey. Figure 1(b) displays the pumped behavior of the respective systems. The equilibrium Fermi level was determined with the pump blocked. In the bulk-conductive case, all pump-induced excitation is contained within 10 ps after the pump pulse and no rigid shift of the bands can be observed. In the bulk-insulating case, a rigid shift of the bands occurs at all delays and is maximal at delay = 0 ps, continuing well beyond 750 ps. This is even more clear in figure 1(c). Only a single 10 ps step at delay = 0 is excited in the bulk-conductive samples. The bulk-insulating samples exhibit chemical potential shifts that decay in both the negative-delay direction and in the positive-delay direction. These spectra were taken with a fluence of approximately 30 μJ cm^{-2}. At this fluence the SPV decay (decay in the positive delay) takes on a two-exponential form with time constants of approximately 50 ps and 5 ns.

We turn our attention to fluence-dependent measurements on the bulk-insulating Bi_2Se_3 in order to investigate effects on the negative delay. Figure 2 summarizes the negative-delay fits as a function of fluence as well as an explanation for the negative-delay profile. Figure 2(a) presents Fermi edge fits to the momentum-integrated delay profiles at multiple fluences and represents the chemical potential shift as a function of delay. The fitting function consists of a Fermi–Dirac distribution multiplied by the sum of a Lorentzian and an affine background. By fitting the chemical potential shifts in the negative delays to an exponential for each fluence we generate figure 2(b), negative-delay time constants as a function of fluence. As the fluence increases, the negative-delay time constants increase as well.

J. Stat. Mech. (2019) 104008

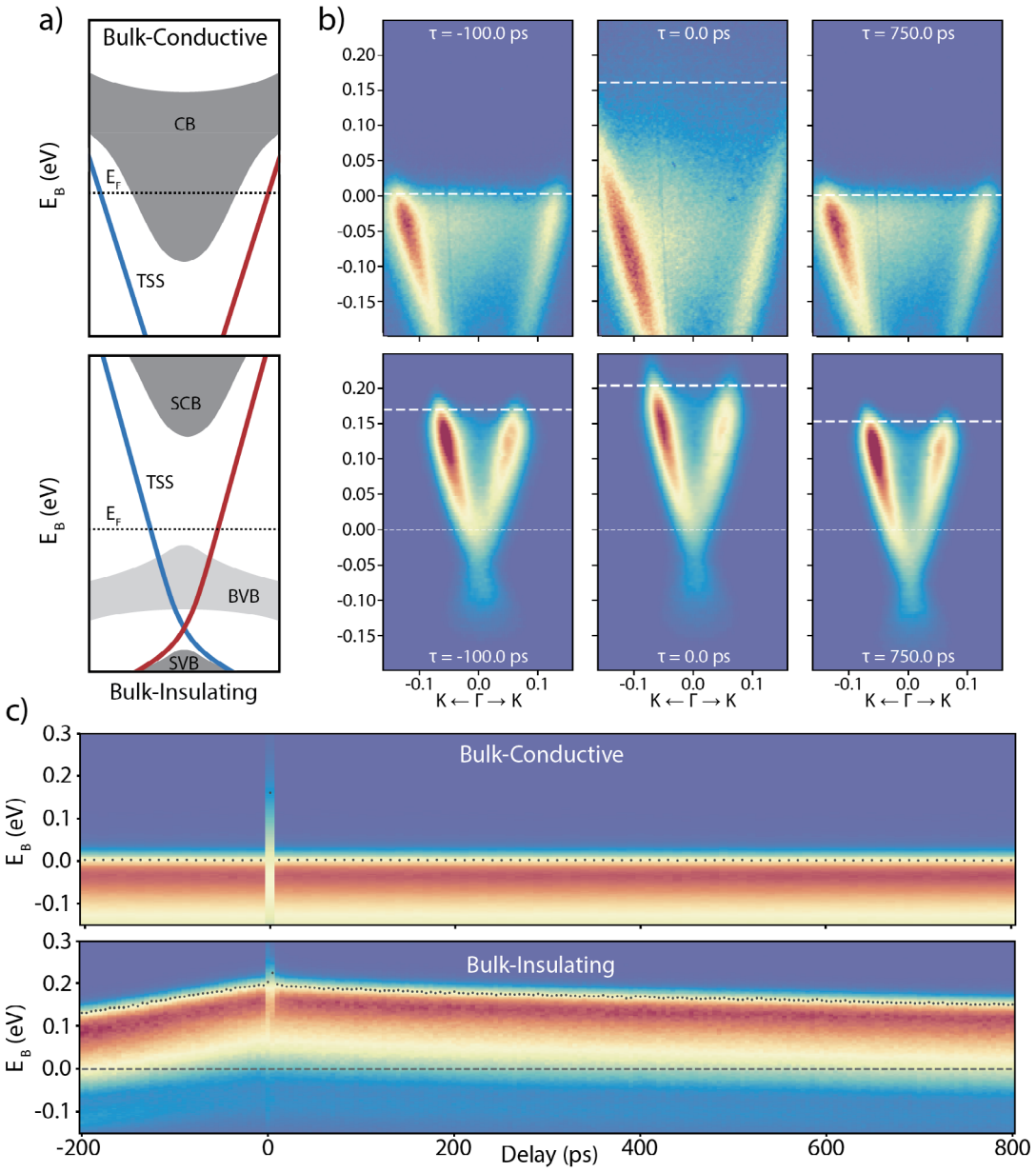

Figure 1. Doping specific SPV generation in Bi_2Se_3. (a) Cartoon band structures for bulk-conductive and bulk-insulating Bi_2Se_3. The insulating films exhibit band bending, shifting the surface conduction and valence bands in dark grey and the topological surface state (TSS) in red and blue. The light grey shape depicts the unshifted bulk valence band. The bulk-conductive sample experiences no band bending as illustrated by no shifting of the conduction band. (b) ARPES spectra at delays −100 ps, 0 ps, and 750 ps demonstrating that only the bulk-insulating samples experience long-lived rigid shifts both in positive and negative delay. (c) Momentum-integrated spectra versus delay. The bulk-conductive sample relaxes within 10 ps where as the bulk-insulating film exhibits a long forward decay and a shorter decay in the negative delay.

J. Stat. Mech. (2019) 104008

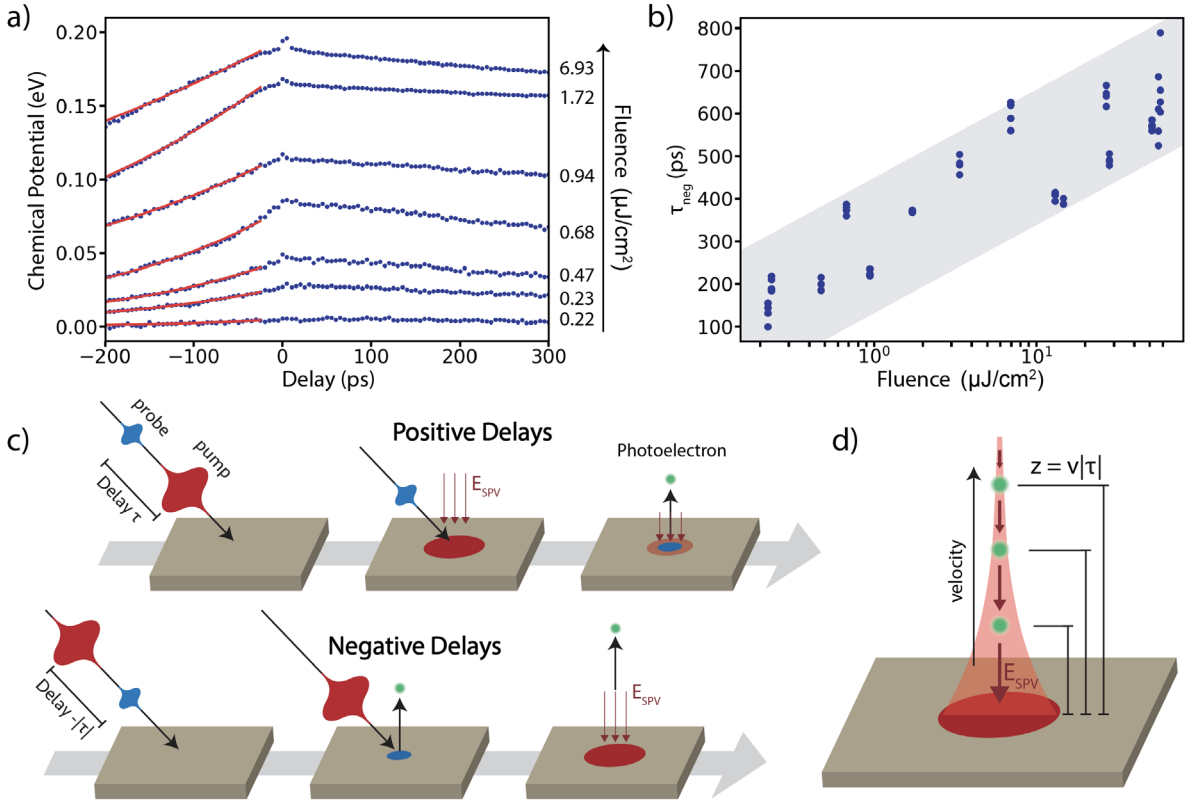

Figure 2. Fitting the negative-delay profiles. (a) Fermi energy fits to momentum-integrated delay profiles at fluences between 0.2 and 7.0 μJ cm^{-2}. The red lines correspond to exponential fits to the negative-delay features. (b) Time constant of negative-delay exponential fits versus fluence displays positive trend, grey region is a guide to the eyes. (c) Comparison between pump–probe dynamics between negative delays and positive delays. Grey arrows corresponds to chronological order of events. (d) Three electrons demonstrate three separate negative delays at the moment of pump excitation. The width of the red-shaded region depicts the electric field strength along the propagation axis. Electrons at larger negative delays sample further segments of the electric field profile.

Figure 2(c) compares the pump–probe interaction between the negative-delay and positive-delay regimes. The positive delay response, in which the pump arrives on the sample at a delay τ before the probe, is most intuitive. In this paradigm, the pump arrives and generates an SPV induced electric field at the surface. At a time $t = \tau$ after the pump, the probe arrives and photoemits an electron. With a sufficiently long SPV lifetime, the electron is effectively photoemitted from a non-grounded plane with a voltage equal to the SPV at the time of photoemission. As a result the spectra at positive delay are rigidly shifted by the magnitude of the SPV at the measured delay, mapping the SPV-decay profile [6–8]. In the case of negative delays, the photoelectron is emitted first, and after time $t = |\tau|$ the pump arrives. By the time the pump arrives, the electron is $z = v|\tau|$ away from the sample surface, where v is the propagation speed. Therefore, the electron experiences the SPV electric field from a distance as determined by the negative-delay value [6–8]. Figure 2(d) demonstrates how three electrons representing three different negative-delay values experience the initial SPV excitation. The

https://doi.org/10.1088/1742-5468/ab458a

J. Stat. Mech. (2019) 104008

width of the red-shaded region corresponds to the strength of the electric field along the propagation axis at a given distance from the sample surface. Each electron samples a different portion of the SPV electric field as they travel to the detector, ultimately leading to a backwards decay profile in the negative-delays of figure 2(a).

Since the negative-delay effect is a result of the photoelectron experiencing the SPV field while enroute to the detector, the SPV-decay time constant might play a role in the fluence dependence of the negative-delay profile, since this would affect the time profile of the observed field. To address this issue, we utilize the model from Yang *et al* [6], which calculates the energy shift of the photoelectron due to a pump-induced dipole. The energy shift at each negative delay ($\Delta E(\tau)$) is determined by integrating the electric field across the path of the photoelectron, parameterized in time.

$$\Delta E(\tau) = -ev \int_0^\infty \varepsilon(v(t + |\tau|), t)\mathrm{d}t. \tag{1}$$

Here, ε is the electric field intensity as a function of space and time and is assumed to have the same time-dependence as the measured SPV decay, such that $\varepsilon(t) \propto \mathrm{e}^{t/\tau_{\mathrm{SPV}}}$.

The spatial portion of the electric field is determined by directly integrating a given spatial dipole distribution ($\mathbf{p}(x, y)$) and only considering normal emission ($\hat{\mathbf{z}}$). The electric field along z is given by:

$$\varepsilon(z) \sim \int \mathrm{d}x\mathrm{d}y \left(\frac{3(\mathbf{p}(x, y) \cdot \hat{\mathbf{r}})\hat{\mathbf{r}} - \mathbf{p}(x, y)}{r^3} \right) \cdot \hat{\mathbf{z}} \tag{2}$$

where $\hat{\mathbf{r}}$ is the vector pointing from a point source $\mathbf{p}(x, y)$ to the photoelectron at $(0, 0, z)$.

We explore this model in figure 3 with multiple pump-beam widths and multiple SPV time constants at a given pump-beam width. Figure 3(a) demonstrates the negative-delay behavior for Gaussian pump-beam widths of $\sigma = 50, 75, 100, 125$, and 150 μm (light teal to dark teal, respectively) and SPV time constants of $\tau_{\mathrm{SPV}} = 100$, 1000, 10 000, 100 000 ps (light red to dark red, respectively). Over many orders of magnitude, there is minuscule dependence of the negative-delay profile on the SPV time constant, implying that the process is mainly driven by the impulse of the initial SPV formation on the photoelectron. On the other hand, the decay profile is significantly modified by small changes in pump-beam spot size as indicated by the evolving green curves and consistent with Yang *et al* [6]. Therefore, the observed dependence of the negative-delay time constant in the measured system in figure 1(b) must be attributed to a fluence-dependent change in the induced dipole geometry.

The scaling of the negative-delay time constant with beam spot size is intuitive. The earlier discussion on the negative-delay response demonstrated that negative-delay values determine the spatial integration region of the electric field. Therefore the negative-delay constant is a measure of the spatial extension of the field [6]. Figure 3(b) illustrates how the length-scale of the field profile depends on the length-scale of the dipole feature. In the limiting case that the SPV is an infinite dipole sheet, the field would be constant with respect to distance from the surface.

The generated dipole geometry should in fact be fluence-dependent [8]. In the case of a linear dependence of SPV amplitude with fluence, a Gaussian pump beam would generate a Gaussian SPV dipole, since all portions of the beam would uniformly scale into

J. Stat. Mech. (2019) 104008

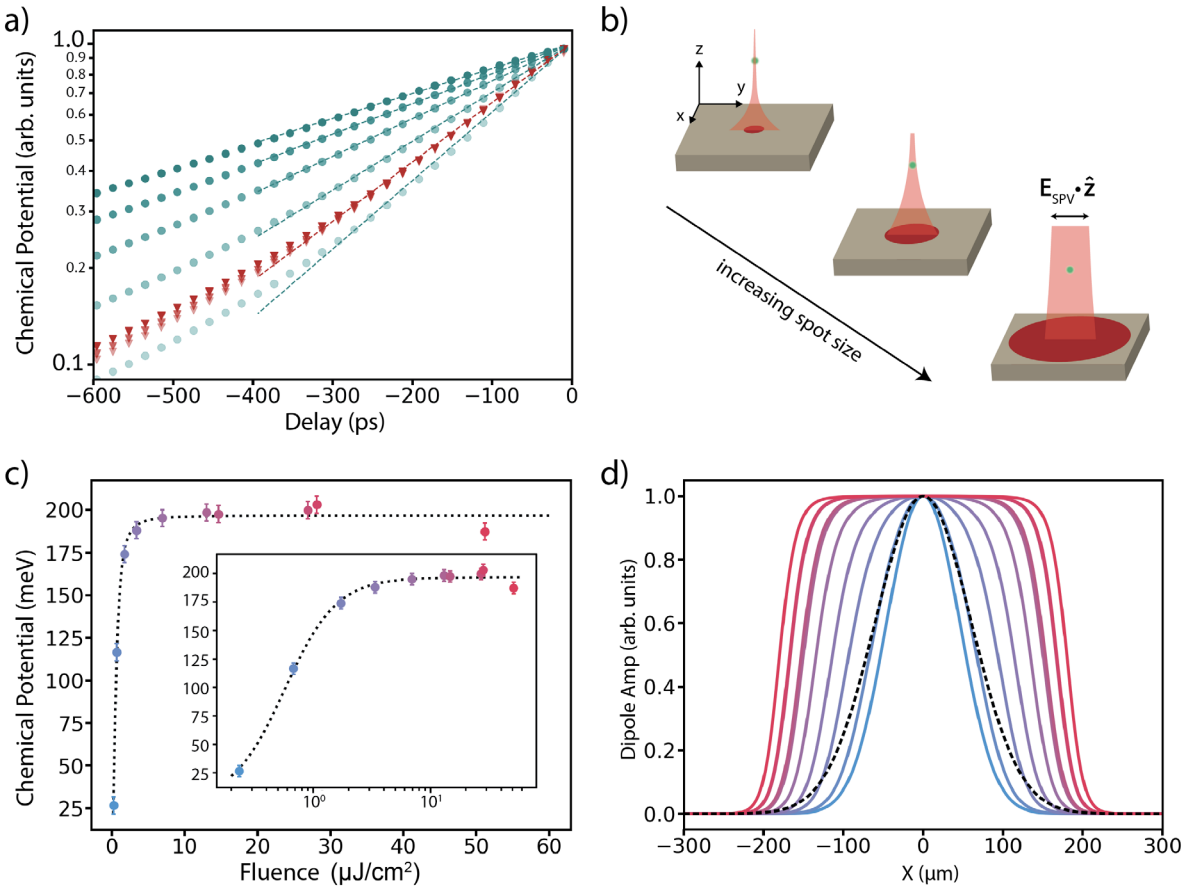

Figure 3. Dipole geometry evaluation. (a) The modeled energy shift versus negative delay as a function of beam size (light teal to dark teal increasing sigma) and forward SPV-decay constant (light red to dark red increasing time constant, *hardly distinguishable*). The shape of the negative delay profile is strongly dependent on beam geometry and largely independent of the SPV time constant. (b) Cartoon depicting the SPV field length-scale as a function of pump-beam diameter. The width of the red-shaded region depicts the magnitude of the SPV field along the z-axis. (c) SPV amplitude as a function of fluence demonstrates heavily non-linear behavior. The dashed black line represents a phenomenological fitting function. Inset: same figure in semi-log plot. (d) Dipole profile as calculated using the SPV amplitude versus fluence response curve. The profile colors correspond to fluences in panel (c), the black dashed curve corresponds to the intial pump profile with $\sigma = 60$ μm.

the dipole profile. However, by fitting the positive delay region with a two-exponential model and summing the respective amplitudes, we see that the SPV amplitude is strongly non-linear in fluence as shown in figure 3(c). The black dashed curve represents a phenomological fit to the fluence of the form $a/(1 + b/x^n)$ ($a = 0.197$, $b = 0.334$, $n = 1.965$). This non-linear scaling of fluence to the SPV dipole would favor top-hat like dipole geometries at high fluence. We can see this clearly by utilizing the SPV fluence response curve from figure 3(c) on the known Gaussian pump with size $\sigma \simeq 60$ μm and the fluences from the study. The evolution of the dipole geometry with fluence is presented in figure 3(d) with colors that correspond to the fluence of the data points

J. Stat. Mech. (2019) 104008

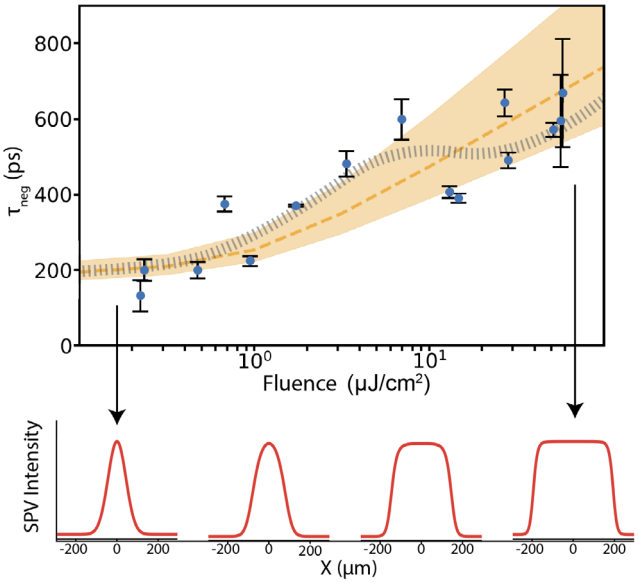

Figure 4. Modeling the dipole fluence dependence. The measured negative-delay time constants as a function of fluence (blue dots) versus the model (yellow region). Errorbars are the standard deviations between multiple measurements at the same fluence. The yellow region was generated by assuming a range of maximal kinetic energies (0.5–0.7 eV) to account for possible changes in work function. The dashed-grey line is a guide to the eyes, illustrating a possible deviating trend. The calculated dipole profiles from 0.1, 1, 10, 100 μJ cm^{-2} demonstrate the evolution of the dipole geometry.

in figure 3(c). The black dashed line depicts the incident Gaussian pump-beam profile. The pump-induced dipole profile transitions from Gaussian-like to top-hat geometry as the fluence is increased.

Figure 4 demonstrates how a non-linear SPV response to fluence can alter the negative-delay profile, matching the field-based calculation closely. By performing the same calculation as above but with $\mathbf{p}(x, y)$ proportional to the augmented dipole profile at fluences ranging between .1 and 100 μJ cm^{-2}, we are able to determine a realistic model of the negative-delay constant versus fluence, displayed as the yellow region. The orange dashed line represents the calculation given a maximal photoelectron kinetic energy of 0.6 eV, the yellow surrounding region contains the results for 0.5–0.7 eV kinetic energies. The maximal kinetic energy is determined by the difference between the work function of the material and the incident photon energy of the probe. In our case, the material work function is approximately 5.4 eV [21, 22] and our photon energy is 5.93 eV. However, changes in surface chemistry can affect the work function of the material [23, 24]. We expect that some of the scatter in the data is due to sample degradation and subsequent changes in work function. However, the deviation from the model (shown in dashed-grey) could reflect real incongruence of the dipole geometry from the calculated profiles. If the surface dipole scaled proportionally with fluence, we would expect a flat response of the decay constant with fluence. The rise in decay constant with increased fluence demonstrates that the non-linear SPV fluence response augments the dipole geometry from approximately Gaussian (left-most red profile) to top-hat (right-most red profile) between the ranges of .1 and 60 μJ cm^{-2}.

J. Stat. Mech. (2019) 104008

Discussion

The negative delays in time-resolved experiments are often ignored, providing only equilibrium information in most scenarios. However, our study demonstrates that negative delays in time-resolved photoemission experiments provide important real-space information in the case of SPV materials. The time-scale of the negative-delay decay reflects the length-scale (from the sample surface) of the pump-induced electric field [6]. In turn, this decay constant can be used to deduce changes in the SPV dipole geometry. The model developed by Yang *et al* and employed on Gaussian pump-beams with linear SPV dipole responses [6], can be generally applied to non-Gaussian pump-beams with non-linear responses. Additionally, this method can be used to verify the incident pump-beam diameter during a T-ARPES experiment. Moreover, with a well calibrated pump beam, it is possible to monitor the work function of an SPV material such as during *in situ* doping.

The evolution of the SPV dipole profile in Bi_2Se_3 from Gaussian to top-hat has strong implications on the dynamics of the excited system. Possible relaxation mechanisms for the SPV excitation include diffusion of the dipole across the surface [11]. Furthermore, free charges can be accelerated along the potential gradient generated by the SPV, facilitating radial spin-currents. The exact kinetics are strongly influenced by the geometry of the SPV dipole field. By determining the initial state of the SPV excitation, one can begin to conjecture on the forces involved during dipole diffusion or charge transfer. For instance, free charges subjected to a top-hat potential will experience much stronger acceleration near the edges than at the center. In fact, charge migration may play a role in the deviations from the model (figure 4 dashed-grey line). At high fluences, charge migration at the edge of the top-hat could reduce the effective size of the dipole on timescales comparable to the negative delay effect, reducing τ_{neg} below the expected values. In terms of device application, the geometry of the pump-induced field determines the geometry of useful devices. For instance, in applications that utilize the SPV as a photoactivated gate, understanding how to produce a uniform electric field from a given pump geometry is crucial.

Conclusion

In conclusion, this study establishes that the negative-delay effect resulting from non-equilibrium time-dependent surface fields can be used to determine the pump-induced field geometry by means of T-ARPES. The first-principles calculation of the energy shift of photoemitted electrons demonstrates that the surface photovoltage geometry on p-type Bi_2Se_3 transitions from Gaussian-like to top-hat as a function of fluence as predicted by the non-linear fluence dependence of the SPV amplitude. This technique can be used as a tool to verify the pump-beam geometry at the focus. More importantly, this method allows for simultaneous collection of real-space and momentum-space information in SPV materials from the typical T-ARPES configuration, introducing a novel procedure to the ARPES tool-kit.

J. Stat. Mech. (2019) 104008

Acknowledgments

The authors would like to thank Kayla Currier, Daniel Eilbott, Nicholas Dale, and Conrad Stansbury for critical discussions on the experiment and analysis. We would also like to thank James Analytis for growing the samples. Both the experimental and theoretical part of this work were primarily supported by the Director, Office of Science, Office of Basic Energy Sciences, Materials Sciences and Engineering Division, of the US Department of Energy, under Contract No. DE-AC02-05CH11231, as part of the Ultrafast Materials Science Program (KC2203). SC was supported by the National Science Foundation Graduate Research Fellowship under Grant No. DGE1852814 and DGE1106400. TM was supported by the EPiQS Initiative of the Gordon and Betty Moore Foundation through Grant No. GBMF4537. AL also acknowledges support from the Gordon and Betty Moore Foundation's EPiQS Grant GBMF4838 that has enabled this research.

Author contributions

SC performed the ARPES measurements and the analysis. TM and JEM contributed to the theoretical framework. AL and SC developed the experiment and AL provided experimental infrastructure and analytical support. All authors contributed to writing the manuscript.

References

[1] Smallwood C L, Jozwiak C, Zhang W and Lanzara A 2012 An ultrafast angle-resolved photoemission apparatus for measuring complex materials *Rev. Sci. Instrum.* **83** 123904
[2] Smallwood C L *et al* 2014 Time- and momentum-resolved gap dynamics in $Bi_2Sr_2CaCu_2O_{8+\delta}$ *Phys. Rev.* B **89** 115126
[3] Jozwiak C *et al* 2016 Spin-polarized surface resonances accompanying topological surface state formation *Nat. Commun.* **7** 13143
[4] Zhang W *et al* 2016 Stimulated emission of Cooper pairs in a high-temperature cuprate superconductor *Sci. Rep.* **6** 29100
[5] Wernet P, Gaudin J, Godehusen K, Schwarzkopf O and Eberhardt W 2011 Femtosecond time-resolved photoelectron spectroscopy with a vacuum-ultraviolet photon source based on laser high-order harmonic generation *Rev. Sci. Instrum.* **82** 063114
[6] Yang S-L, Sobota J A, Kirchmann P S and Shen Z-X 2013 Electron propagation from a photo-excited surface: implications for time-resolved photoemission *Appl. Phys.* A **116** 85–90
[7] Ulstrup S *et al* 2015 Ramifications of optical pumping on the interpretation of time-resolved photoemission experiments on graphene *J. Electron Spectrosc. Relat. Phenom.* **200** 340–6
[8] Tanaka S-I 2012 Utility and constraint on the use of pump–probe photoelectron spectroscopy for detecting time-resolved surface photovoltage *J. Electron Spectrosc. Relat. Phenom.* **185** 152–8
[9] Yoshikawa T *et al* 2018 Enhanced photovoltage on the surface of topological insulator via optical aging *Appl. Phys. Lett.* **112** 192104
[10] Ishida Y *et al* 2015 Emergent photovoltage on smb6 surface upon bulk-gap evolution revealed by pump-and-probe photoemission spectroscopy *Sci. Rep.* **5** 8160
[11] Neupane M *et al* 2015 Gigantic surface lifetime of an intrinsic topological insulator *Phys. Rev. Lett.* **115** 116801
[12] Kronik L and Shapira Y 1999 Surface photovoltage phenomena: theory, experiment, and applications *Surf. Sci. Rep.* **37** 1–206

[13] Schroder D K 2001 Surface voltage and surface photovoltage: history, theory and applications *Meas. Sci. Technol.* **12** R16
[14] Fu L, Kane C L and Mele E J 2007 Topological insulators in three dimensions *Phys. Rev. Lett.* **98** 106803
[15] Hsieh D *et al* 2009 A tunable topological insulator in the spin helical Dirac transport regime *Nature* **460** 1101–5
[16] Moore J E 2010 The birth of topological insulators *Nature* **464** 194–8
[17] Li C H *et al* 2014 Electrical detection of charge-current-induced spin polarization due to spin-momentum locking in Bi_2Se_3 *Nat. Nanotechnol.* **9** 218
[18] McIver J W, Hsieh D, Steinberg H, Jarillo-Herrero P and Gedik N 2012 Control over topological insulator photocurrents with light polarization *Nat. Nanotechnol.* **7** 96–100
[19] Zhang H *et al* 2014 Anomalous photoelectric effect of a polycrystalline topological insulator film *Sci. Rep.* **4** 5876
[20] Yao J D, Shao J M, Li S W, Bao D H and Yang G W 2015 Polarization dependent photocurrent in the Bi_2Te_3 topological insulator film for multifunctional photodetection *Sci. Rep.* **5** 14184
[21] Edmonds M T *et al* 2014 Air-stable electron depletion of Bi_2Se_3 using molybdenum trioxide into the topological regime *ACS Nano* **8** 6400–6
[22] Suh J *et al* 2014 Fermi-level stabilization in the topological insulators Bi_2Se_3 and Bi_2Te_3: origin of the surface electron gas *Phys. Rev.* B **89** 115307
[23] Edmonds M T *et al* 2014 Stability and surface reconstruction of topological insulator Bi_2Se_3 on exposure to atmosphere *J. Phys. Chem.* C **118** 20413–9
[24] Kahn A 2016 Fermi level, work function and vacuum level *Mater. Horiz.* **3** 7–10

J. Stat. Mech. (2019) 104008